Oxidative Immobilization of Gaseous Mercury by [Mo₃S(S₂)₆]²⁻ Functionalized Layered Double Hydroxide

Subrata Chandra Roy,^a Abu Asaduzzaman,^b Brooklynn May,^a Airin M. Beals,^a Xinqi Chen,^c Xianchun Zhu,^d Saiful M. Islam*^a

^aDepartment of Chemistry, Physics, and Atmospheric Sciences, Jackson State University, Jackson, MS, 39217, USA ^bSchool of Science, Engineering and Technology, Pennsylvania State University - Harrisburg, Middletown, PA 17057,USA ^cNUANCE Center, Northwestern University, Evanston, IL-60208, USA

^dDepartment of Civil Engineering, Jackson State University, Jackson, MS, 39217, USA

Abstract:

Every year, thousands of tons of gaseous mercury are released globally, prompting the World Health Organization (WHO) in 2020 to designate mercury as one of the top 10 chemicals posing severe health risks. Therefore, the removal of Hg⁰ from the environment is imperative. Our study introduces $[Mo_3S(S_2)_6]^{2-} \equiv [Mo_3S_{13}]^{2-}$ functionalized layered double hydroxides nanoparticles, (LDH-Mo₃S₁₃), as an excellent sorbent for gaseous Hg⁰. This material achieved a remarkable sorption capacity of $\sim 2.33 \times 10^3$ mg/g for gaseous elemental Hg⁰. Such an enormously high sorption capacity makes this material the lead non-platinum-based Hg⁰ gas sorbent known to date. Though sulfides of the Mo₃S(S₂)₆ species of the LDH predominantly serve as active sites for capturing gaseous Hg, their integration is essential for the accessibility of gaseous Hg⁰ to the individual reactive active site between the LDH lamella. A heterogeneous reaction between the gaseous Hg⁰ vapor and the solid LDH-Mo₃S₁₃ sorbent enables the oxidation of gaseous Hg⁰ to Hg²⁺ and the reduction of the S₂²⁻ groups to 2S²⁻ yield redox-driven formation of the nanocrystalline HgS onto the solid sorbents. Density Functional Theory (DFT) calculations provide further insights into the interactions between Hg⁰ and S indicating adsorption energy ranging from -8 kJ/mol to -19 kJ/mol. Moreover, the overall reaction enthalpy was calculated as -4048 kJ/mol, suggesting the spontaneous formation of HgS. This investigation unveils an atomistic understanding of the redox-driven interactions between Hg⁰ vapor and Mo₃S(S₂)₆ species, as well

as the remarkably high mercury sorption capacity of LDH—Mo₃S₁₃, highlighting the potential of metal sulfide functionalized LDHs for the efficient immobilization of gaseous elemental mercury.

INTRODUCTION

The anthropogenic mercury (Hg) emissions, estimated at around 2 Gg·yr⁻¹ (Gg: Gigagram or 1000 tons), far exceed natural emissions by over tenfold. ¹⁻⁴ Exposure to methylmercury poses risks to approximately 75,000 newborns annually in the United States, leading to developmental delays or disabilities during pregnancy. ⁵ Since the industrial era began (~1850) until 2010, North America has had the highest (30%) cumulative mercury discharges to the environment. ⁶ The lifetime of atmospheric mercury against removals, such as deposition and recycling, is about six months, allowing transport on a hemispheric to global scale. ^{1,3,7} The atmospheric mercury drops down to soil and surface waters, ⁸ where bacterial activities contribute to the formation of neurotoxic methyl mercury, which subsequently accumulates in humans and animals via the food chain. ^{9,10} The severe noxiousness of mercury enforces the US EPA to designate it as a highly toxic and hazardous air pollutant under the Clean Air Act Amendments (CAAA). ¹¹

Mercury enters into the atmosphere through both natural and anthropogenic activities. The natural process includes volcanism, weathering of Hg-containing rocks, and geothermal activity¹² while anthropogenic activities include coal and fuel-based powerplants, mining, incinerators (e.g., medical, urban, and rural wastes), industry (e.g., metal manufacturing, caustic soda manufacturing, cement)^{4,13–15} and Hg-containing appliances (e.g., batteries, compact fluorescent lamps, liquid crystal display (LCD) screens, dental amalgam, barometer, and thermometer) release Hg⁰ to the environment, including air, soil, and water. ¹⁶ Importantly, elemental mercury (Hg⁰), which is emitted from coal combustion and raw natural gas, is the major source of gaseous mercury in the atmosphere. ^{17,18} Besides the widespread emission of Hg⁰ gas in the atmosphere, mercury is a problematic element in the defense of legacy nuclear wastes. ¹⁹ Through the nuclear waste treatment process, Hg enters into the Waste Treatment Plants (WTP) as an off-gas condensate waste stream during the high-temperature vitrification process. ²⁰ The efficient removal of Hg⁰ from the gaseous medium is bottlenecked by efficient methods and materials. ²¹ Various sorbents, for example, activated carbon, ²² modified red mud from the alumina industry, ²³ iodine-iodate, ²⁴

bio-char,²⁵ mixed-transition metal oxides,^{26–28} spinal-based catalysts,^{29–31} Cu²⁺ enhanced Fenton process,³² are known to remove mercury elemental gaseous Hg⁰. Although activated carbon is the most commonly used sorbent for the removal of gaseous mercury,³³ its poor affinity to Hg⁰ limits the removal capacity.^{28,34,35} In contrast, sulfur-impregnated activated carbon, various metal sulfides,³⁶ sulfur-containing composite material,^{37,38} and sulfide-functionalized materials, such as Cu-doped silica,³⁹ Co-doped iron nanoparticles,⁴⁰ porous silica,⁴¹ and SiO₂-TiO₂ nanocomposite⁴² deliver notable affinity to bind the mercury.

Previous reports show that layered double hydroxides functionalized with polysulfides, LDH $-S_x$ ($x \sim 4$ and 6), and NiAl $-S_4$ –LDH@SiO₂ is an efficient sorbent for the removal of elemental mercury vapor, where S_x^{2-} chain is important to enhance its efficiencies. Later, Xu, et al. reported [MoS₄]²⁻ functionalized LDH as an efficient sorbent gaseous elemental mercury, which further demonstrated the synergy of the sulfide functionalized LDHs toward the capture of gaseous Hg. In these materials, the positively charged lamellar of the LDH nanosheet provides the stability of the S_x^{2-} and MoS_4^{2-} anions by the intercalation of the corresponding ions. Hence, a soft polarizable Lewis basic nature of the sulfide species offers a strong chemical intuition to bind mercury via Hg-S covalent interactions. This chemical interaction is mainly governed by Pearson's hard-soft acid-base paradigm. Thus, one may surmise that a high density of sulfide per formula unit of LDHs introduces a high density of active sites for mercury.

Here, we report that $Mo_3S_{13}^{2-} \equiv [Mo_3S(S_2)_6]^{2-}$ functionalized MgAl—LDH nanoparticles, which we refer to as LDH— Mo_3S_{13} , is an efficient sorbent for gaseous Hg^0 . The $Mo_3S_{13}^{2-}$ ion possesses a high density of disulfides (S_2^{2-}) that undergoes a reduction to mono-sulfide $(S_2^{2-} \rightarrow 2S^{2-})$ with concurrent oxidation of gaseous elemental Hg ($Hg^0 \rightarrow Hg^{2+}$) yielding HgS nanoparticles. By DFT calculation, we showed that the reaction enthalpy for the heterogeneous redox reaction between gaseous elemental Hg^0 and sulfides of the solid LDH— Mo_3S_{13} is -4048 kJ/mol and thus favors immobilizing gaseous Hg^0 by the formation of thermodynamically stable HgS nanoparticles. Here, the hard-soft Lewis acid-base (HASB) interaction between the soft polarizable Lewis base (S^{2-}) and Lewis acid (Hg^{2+}) is the crucial impetus for the immobilization of gaseous elemental mercury.

EXPERIMENTAL

Material synthesis

MgAl—CO₃ (LDH—CO₃), and MgAl—NO₃ (LDH—NO₃) were synthesized by solvothermal and ion exchange methods, respectively according to our previous report⁴⁷. The anionic precursor of [Mo₃S₁₃]²⁻ was obtained in the form of (NH₄)₂[Mo₃S(S₂)₆]·H₂O which was also produced by solvothermal technique as described in the literature.⁴⁸ The functionalized sorbent material, MgAl—Mo₃S₁₃ (LDH—Mo₃S₁₃) was synthesized as described in the past.⁴⁹ Typically, 0.20 g of LDH—NO₃ was sonicated for 1 hour in 7.5 mL of dimethylformamide (DMF) to exfoliate the positively charged 2D layers of LDH. Afterward, 0.02 g of [Mo₃S₁₃]²⁻ dispersed in 7.5 mL DMF was added to the exfoliated LDH solution and stirred for 24 h. The resulting brown solid of LDH—Mo₃S₁₃ was centrifuged, washed with DIW, and acetone, and dried at room temperature and pressure. Powder X-ray diffraction, (XRD); Fourier Transform Infrared Spectroscopy, (FTIR); and Energy Dispersive Spectroscopy, (EDS) analysis confirm the functionalization of LDH—NO₃ with the [Mo₃S₁₃]²⁻ anion.

Mercury vapor capture experiments

The Mercury vapor capture experiment was conducted by the cone method in a closed vial with functionalized adsorbent material, LDH $-Mo_3S_{13}$, S LDH-NO3, and (NH₄)₂Mo₃S₁₃ as described in SI.

Computational Methodology

Calculations were performed using electronic structure density functional theory (DFT) using plane wave basis sets as implemented in the software VASP (Vienna ab initio simulation package) version 5.4.1.^{50,51} The exchange-correlation contribution to the total energy is modeled using the generalized-gradient approximation (GGA) functional. The orbital interactions are analyzed by the projector-augmented-wave method (PAW)⁵², specifically utilizing Perdew-Burke-Ernzerhof (PBE)⁵³, pseudopotentials provided by VASP. Using pseudopotentials ensures a scalar relativistic approach is included in the calculations. The energy cutoff was set to 500 eV to maximize the completeness of the plane-wave basis sets. The Monkhorst-Pack k-point grid was set to gamma point only.⁵⁴ The convergence criterion for local energy minima is that all atomic forces be smaller than 0.02 eV/Å. All calculations were performed using the supercell approach using a simulation box of 30 × 30 × 30 Å.

RESULTS AND DISCUSSION

Synthesis and Characterization

MgAl—Mo₃S₁₃ layered double hydroxides (LDH—Mo₃S₁₃) were synthesized at room temperature by the intercalation of Mo₃S(S₂)₆ \equiv [Mo₃S₁₃] anion into the positively charged layers of the host LDH—NO₃ following by anion exchange method (Figure 1A), as described previously.⁴⁹ Energy dispersive spectroscopy (EDS) shows a uniform distribution of Mg, Al, Mo, and S throughout the pristine material, LDH—Mo₃S₁₃ (Figure 1B-G). Atomic abundances were determined using semiquantitative surface analysis by EDS, which revealed 17.74, 11.00, 61.71, and 9.55 in percentage for Mg, Al, S, and Mo, respectively.

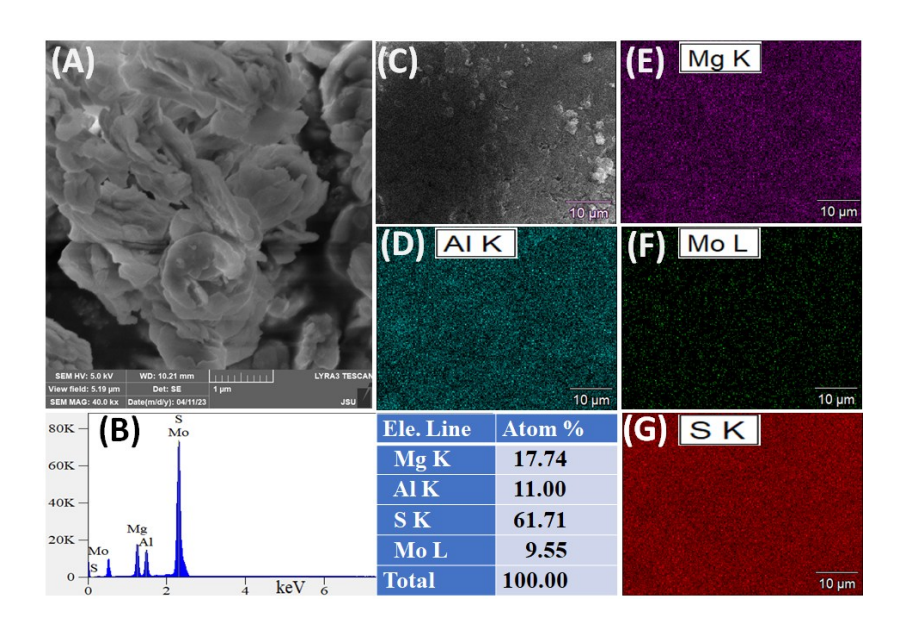


Figure 1. SEM image (A), EDS spectra, and elemental composition (B) of the pristine LDH—Mo₃S₁₃, image (C) showing the materials used for elemental mapping (D-G) which demonstrated a homogeneous distribution of the elements, Mg, Al, Mo, and S.

Interactions of Gaseous Mercury with LDH-Mo₃S₁₃

Experiments for capturing mercury vapor were conducted in closed vials using LDH—Mo₃S₁₃, LDH—NO₃, and (NH₄)₂Mo₃S₁₃ as sorbents (Table 1). This experiment was conducted using the experiment as shown in Figure 2. To determine the sorption efficiency of Hg⁰ vapor, we introduced about 45 mg of LDH—Mo₃S₁₃ in a cone-shaped filter paper which was then placed in a vial that contained liquid elemental Hg. Afterward, the liquid Hg containing the closed vial was heated at 145 °C to transform it to a gaseous state. The gaseous Hg⁰ penetrates the filter

paper to react with sorbent materials. Similar experiments were conducted for LDH—NO₃ and (NH₄)₂Mo₃S₁₃ that we used as controls. Among them, LDH—Mo₃S₁₃ showed a color change from radish-brown to a black hue after being exposed to gaseous Hg, suggesting a chemical interaction involved between Hg⁰ and LDH—Mo₃S₁₃ (Figure 3A inset, and Table 1). The capture of gaseous elemental Hg⁰ was further understood by an increase in the amount of mass of the sorbents, where only LDH—Mo₃S₁₃ showed a substantial mass increase, as shown in Table 1.

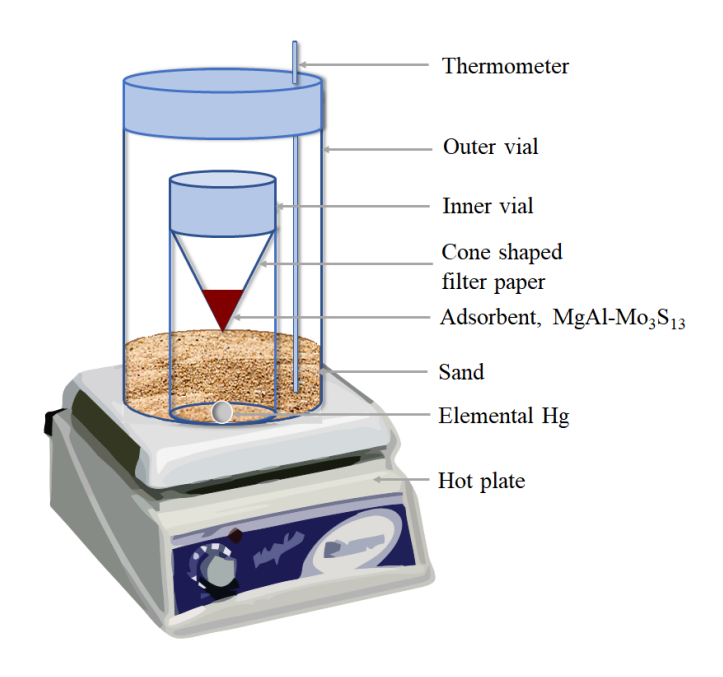


Figure 2. Schematic diagram of cone technique for mercury vapor capture experiment.

Table 1. Details of gaseous Hg⁰ sorption experiment by different sorbent materials (reaction temp. 145 °C).

Sorbent	Time	Amount of	Weight	Sorption	Color change
	(h)	sorbent (mg)	gain (mg)	capacity (mg/g)	
LDH-Mo ₃ S ₁₃	3	45.40	56.70	1248.9	Radish-brown → blackish
LDH-Mo ₃ S ₁₃	24	45.50	72.00	1582.4	Radish-brown → blackish
LDH-Mo ₃ S ₁₃	48	45.50	106.20	2334.1	Radish-brown → black hue
LDH-NO ₃	48	45.71	5.73	125.4	White → white
$(NH_4)_2Mo_3S_{13}$	48	45.60	5.08	111.4	Orange → orange

The sorption of gaseous Hg⁰ by LDH-Mo₃S₁₃ is mainly attributed to the interactions of the sulfides of $[Mo_3S_{13}]^{2-}$. The $[Mo_3S_{13}]$ anion consists of three Mo^{4+} ions, six disulfides (S_2^{2-}) , and one apical sulfide (S²⁻). Each Mo⁴⁺ ion is attached to an apical (S²⁻)_{ap} anion and further coupled to each other via bridging disulfide (S₂²-)_b groups. ^{48,55} Additionally, each Mo⁴⁺ ion is bonded to a terminal disulfide (S22-)t group. According to SEM/EDS (Figure 1B, and Table S1), the atomic abundance of Mg: Al is 0.62: 0.38. and the molar ratios of Mo/Mg and Mo/Al are 0.54 and 0.87, respectively. Considering the amount of trivalent A1³⁺ ions, the maximum 0.19 moles of [Mo₃S₁₃]²⁻ can be inserted into the LDH. Therefore, the molecular formula of LDH-Mo₃S₁₃ would be $Mg_{0.62}Al_{0.38}(OH)_2(Mo_3S_{13})_{0.11}(NO_3)_x(CO_3)_{0.08-x/2} \cdot H_2O$ (where x = 0.0 to 0.16). On the other hand, according to ICP-MS (Table S1), the molar ratio of Mg: Al is 0.63: 0.37 which is very close to the SEM/EDS results, and the Mo/Mg and Mo/Al molar ratios are 0.67 and 1.14, respectively. Therefore, the molecular formula of LDH-Mo₃S₁₃ would be Mg_{0.63}Al_{0.37}(OH)₂(Mo₃S₁₃)_{0.14}(NO₃)_x $(CO_3)_{0.045-x/2}$ ·H₂O; where x = 0 - 0.090 and MW is ~178.5 g/mol. Hence, the ICP-MS analysis of LDH-Mo₃S₁₃ revealed a nearly complete exchange of NO³⁻ by the [Mo₃S₁₃]²⁻ or in other words, the presence of a very low content of carbonate, (CO₃)²- and/or nitrate (NO₃)². The strong affinity of divalent CO₃²⁻ and the large steric hindrance of [Mo₃S₁₃]²⁻ might prevent its complete exchange with NO₃^{-.56,57} Hence, the amount of apical, bridging, and terminal sulfur (S₂²⁻)_{b,t} in each gram of LDH-Mo₃S₁₃ is $\{(13\times0.14/178.5)$ moles = $\{1.02\times10^{-2}\}$ moles. Therefore, the theoretical mercury sorption capacity of one gram of LDH-Mo₃S₁₃ is $(1.02\times10^{-2} \text{ mol}\times200.5 \text{ g/mol}) = 2.04\times10^{3} \text{ mg}$. However, the experimental sorption capacity value obtained in this study is 2.33×10^3 mg/g, a little higher than the theoretical value. The slightly higher (14%) sorption capacity of LDH-Mo₃S₁₃ might be attributed to the physisorption capacity of mercury vapor as well as the sorption ability of the host material; LDH-NO₃ likewise demonstrates the mercury vapor capture capacity (Table 1).

The experimental sorption capacity of LDH—Mo₃S₁₃ for gaseous mercury is about 18.6 and 21 times greater than LDH—NO₃ and (NH₄)₂Mo₃S₁₃, respectively. Specifically, the Hg⁰ sorption capacity for LDH—NO₃ and (NH₄)₂Mo₃S₁₃ was obtained as 125.4 and 111.4 mg/g, respectively (Table 1). The control experiments reveal that, to a certain extent, the active sites, Mo₃S(S₂)₆ in the (NH₄)₂Mo₃S₁₃ interact with the gaseous Hg. However, this interaction is constrained by its bulk structure which is attributed to a low surface-to-volume ratio. In contrast, the sorption capacity of LDH—NO₃ is very low due to the absence of active sites. This control

experiment suggests that the hydroxyl group has an insignificant affinity to bind gaseous Hg⁰ which is in agreement with previous reports.^{21,38} Hence, physisorption can play a role in adsorbing a small quantity of gaseous Hg⁰, as we see for LDH—NO₃. Our experiments suggest that nanoparticles of two-dimensional LDH functionalized with a (di)sulfide-rich thio-molybdate anion of Mo₃S(S₂)₆ significantly boost the sorption efficiency of gaseous Hg. Here the channels among the host LDH layers allow the gaseous Hg⁰ to penetrate the layers where it comes into contact with individual guest Mo₃S(S₂)₆ ions to initiate the heterogenous reactions with sulfide ions.

Table 2 shows a comparable Hg⁰ sorption capacity of LDH-Mo₃S₁₃ with the other highperforming sorbents. Among these, LDH-Mo₃S₁₃ stands out among the top sorbents for gaseous mercury. Although the aerogel of K-Pt-S_x has a higher sorption capacity, ³⁵ the presence of Pt and the fabrication of aerogels by supercritical drying make this material extremely expensive. These ultimately bottlenecked its widespread use on industrial scales. The polysulfide intercalated LDH, LDH $-S_x$ (x = 2,4,5) also showed good Hg⁰ sorption capacity, which is about 43% less than the LDH-Mo₃S₁₃; however, a high propensity of the oxidation of the polysulfide group and the synthetic complexities of the precursor polysulfides species limits its practical use. Sulfide species present in LDH-Mo₃S₁₃ and LDH-S_x are the active sites for mercury vapor capture. Compared to LDH-S_x, LDH-Mo₃S₁₃ resulted in superior sorption capacity for gaseous Hg⁰ capture, which is attributed to the increased number of active sites (4 times higher). Besides, LDH-S_x and other highly performing materials, specifically chalcogels, contain polysulfide species that are prone to easy oxidation, resulting in a loss of Hg⁰ sorption capacity. In contrast, the Mo₃S₁₃ cluster itself remains stable due to the unique bonding nature of the bridging and terminal disulfide (S_2^{2-}) with Mo⁴⁺ cations in the trinuclear molybdenum cluster. Hence, the synergistic role of Mo-S covalent interactions and the intercalation of Mo₃S₁₃ in the host LDH layers implies superior stability of the hybrid LDH-Mo₃S₁₃. This, coupled with its scalable synthesis and remarkably higher sorption capacity, positions this material as a promising sorbent for atmospheric mercury.

Sulfide-based materials, such as MoS₄-bridged CoFe layer double hydroxides,³⁸ Cu–S–Fe,⁴⁰ CuS,⁵⁸ and have already been reported for the removal of Hg⁰ from flue gas. From this perspective, one may surmise that LDH-Mo₃S₁₃ could be efficient for the removal of mercury from flue gas. Besides, this material should find application in natural gas purification and the removal of gaseous mercury from off-gas nuclear waste condensate streams. A synergy of the extraordinary capacity of LDH-Mo₃S₁₃ and the design of innovative reactors could deliver an

unprecedented opportunity for the capture of Hg. However, further exploration of these applications is beyond the scope of the current effort.

Table 2. Comparison of sorption capacity of LDH—Mo₃S₁₃ with the other reported materials.

Sorbent	Sorption capacity (mg/g)	Ref.
MgAl-Mo ₃ S ₁₃ -LDH	2.33×10^3	This work
S_x —LDH (x = 2,4,5)	$(0.59-1) \times 10^3$	21
CoFe—MoS ₄ —LDH	16.39	38
NiAl—S ₄ —LDH@SiO ₂	7.7	43
Aerogel, MoS _x	2.0×10^3	59
Metal-chalcogenide aerogel, K—Pt—S _x	$(0.43-5.45) \times 10^3$	35
Chalcogel, Zn-[SnS ₄]	29.4	35,60
DMF inserted MoS ₂	27.40-46.91	61
Colloidal CuS	736.5	58
CuS / Polyurethane foam	265.60	62
CuS-Doped Ti ₃ C ₂ MXene Nanosheets	20.47	63
S functionalized Cu doped porous silica, Cu—S—Si	19.8	39
S functionalized Cu doped Fe-NP, Cu-S-Fe	0.17-2.73	40
S-impregnated activated carbon, PILOT5_S400	1.44	46
Chitosan nanofilled GO	381	64

Mechanistic Investigations of the Gaseous Hg⁰ Sorption

Thermal analysis of the pristine and post Hg-sorbed LDH—Mo₃S₁₃ showed initial weight loss of 13 and 15.5% at 245 °C, respectively (Figure S1). This may be attributed to the evaporation of intercalated and surface water. At about 450 °C, the post-treated LDH—Mo₃S₁₃ loses about 40.7% of the total weight, while the pristine LDH—Mo₃S₁₃ loses ~21.3% at 500 °C. The weight loss for the post Hg-sorbed samples is approximately twice that of the pristine LDH—Mo₃S₁₃. The excessive weight loss for the post-interacting LDH—Mo₃S₁₃ with gaseous Hg⁰ may be related to the sublimation of HgS. The quantitative chemical analysis of the TGA treated of Hg⁰ sorbed LDH—Mo₃S₁₃ by EDS supports this assessment (Figure S2).

X-ray powder diffraction of the post interacted LDH—Mo₃S₁₃ (Figure 3A) reveals highly intense peaks at $2\theta \sim 26.23$ (111), 30.43 (200), 43.67 (220), and 51.80 (311), which confirms the presence of HgS.⁶⁵ Hence, the formation of HgS infers the oxidative separation of gaseous Hg⁰ during the interactions with LDH—Mo₃S₁₃. In particular, the oxidative conversion of gaseous elemental mercury into mercuric ion, Hg⁰ \rightarrow Hg²⁺ + 2e⁻ is compensated by the simultaneous reduction of disulfide to sulfide, (S₂²⁻)_{b,t} + 2e⁻ \rightarrow 2S²⁻. Such a redox reaction is plausibly attributed to the formation of solid HgS particles (Eq. 1). It is worth mentioning that the LDH structure remains stable after the sorption reaction. The stability of the LDH structure can be attributed to the formation of LDH—SO₄ and/or LDH—MoO₄ by the oxidation of some sulfides, probably the apical sulfide (S²⁻) and Mo⁴⁺ ions into [S^{VI}O₄]²⁻ and [Mo^{VI}O₄]²⁻, respectively (Eq. 2).

$$nHg^0 + [Mo_3^{IV}S(S_2)_6]^{2-} \rightarrow nHgS + (13-n)S^{z-} + 3Mo^{IV}$$
 (z = 1and/or2) Eq. 1

$$(13-n)S^{z-} + 3Mo^{IV} + 8O_2 \xrightarrow{LDH-Layer(air\ oxid.)} LDH-SO_4 + 3LDH-(MoO_4)$$
 Eq. 2

In contrast to LDH—Mo₃S₁₃, XRD of the post-interacted (NH₄)₂Mo₃S₁₃ showed HgS peaks (Figure S3). This suggests that Hg···S interaction is the dominant mechanism to immobilize gaseous Hg⁰, however, the lower density of the active sites at the surface of the bulk (NH₄)₂Mo₃S₁₃ crystals limits the Hg⁰ sorption capacity. The post-interacted LDH—NO₃ shows no HgS peaks but very weak peaks of an unknown phase at $2\theta \sim 29.79$ and 31.91° .

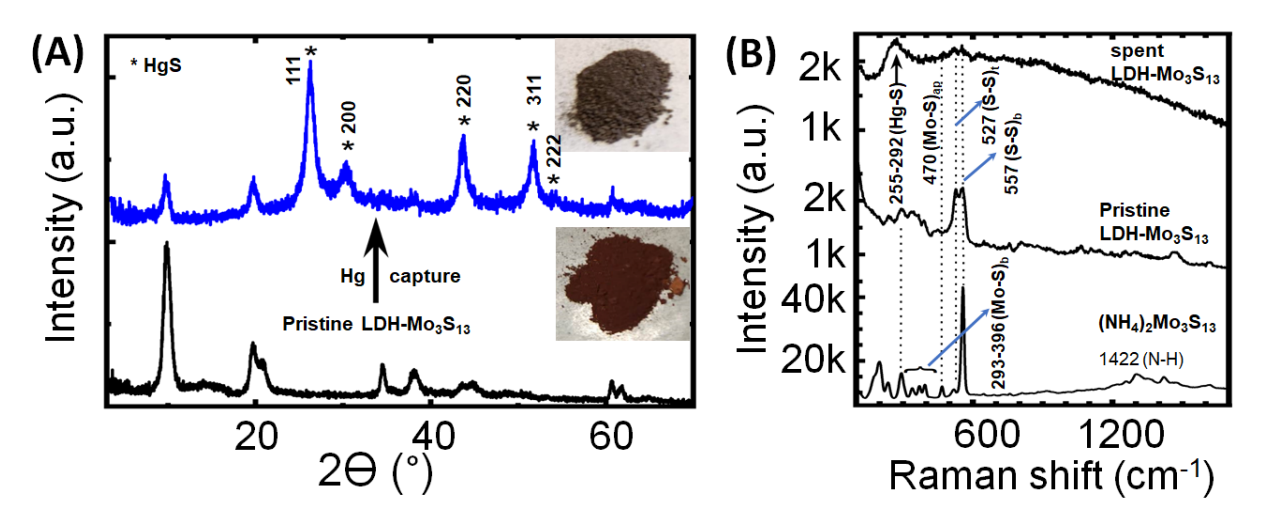


Figure 3. Powder X-ray diffraction of the pristine and post-treated LDH—Mo₃S₁₃ (A) inset the color changes after interactions with gaseous Hg⁰; asterisks show the X-ray diffraction peaks of

HgS; Raman spectra (B) of $(NH_4)_2Mo_3S_{13}$, pristine and Hg^0 sorbed LDH— Mo_3S_{13} implying the abolish of $(S-S)_b$ bond and formation of Hg-S bond in the post-treated sample.

Raman spectrum of the pristine LDH— Mo_3S_{13} showed all the vibrational peaks that belong to $[Mo_3S(S_2)_6]^{2-}$ group (Figure 3B) as reported in the literature. ^{66–69} The bridging (S-S)_b, terminal (S-S)_t, apical (Mo-S)_{ap}, and (Mo-Mo) vibrational modes were observed at 557, 527, 470, and 237 cm⁻¹, respectively. Moreover, the (Mo-S)_b modes are observed in the range of 293-396 cm⁻¹. Raman spectrum of Hg^0 gas treated LDH— Mo_3S_{13} showed the characteristics (S-S)_b, (S-S)_t, and (Mo-S)_{ap} vibrational modes, but their intensities decrease almost close to the background spectrum and thus could be negligible. This experiment suggests that the reductive conversion of S_2^{2-} into S^{2-} led to the formation of HgS, which is discussed in Equation 1. Moreover, the presence of the vibrational bands at the range of 255 to 292 cm⁻¹ of the post-interacted LDH— Mo_3S_{13} confirms the formation of HgS.

EDS spectrum (Figure 4A) of the post-sorbed solids demonstrates the presence of Hg⁰ along with Mg, Al, Mo, and S, while the SEM image (Figure 4B) shows the retention of the platelike morphology of the crystallites. TEM images of untreated materials (Figure 4C) revealed an ultrathin nano-sheet of single-phase LDH—Mo₃S₁₃, whereas the gaseous Hg⁰ treated sample clearly shows the presence of a second phase (Figure 4D). This second phase is HgS was formed by the interactions of gaseous Hg⁰ with LDH-Mo₃S₁₃.

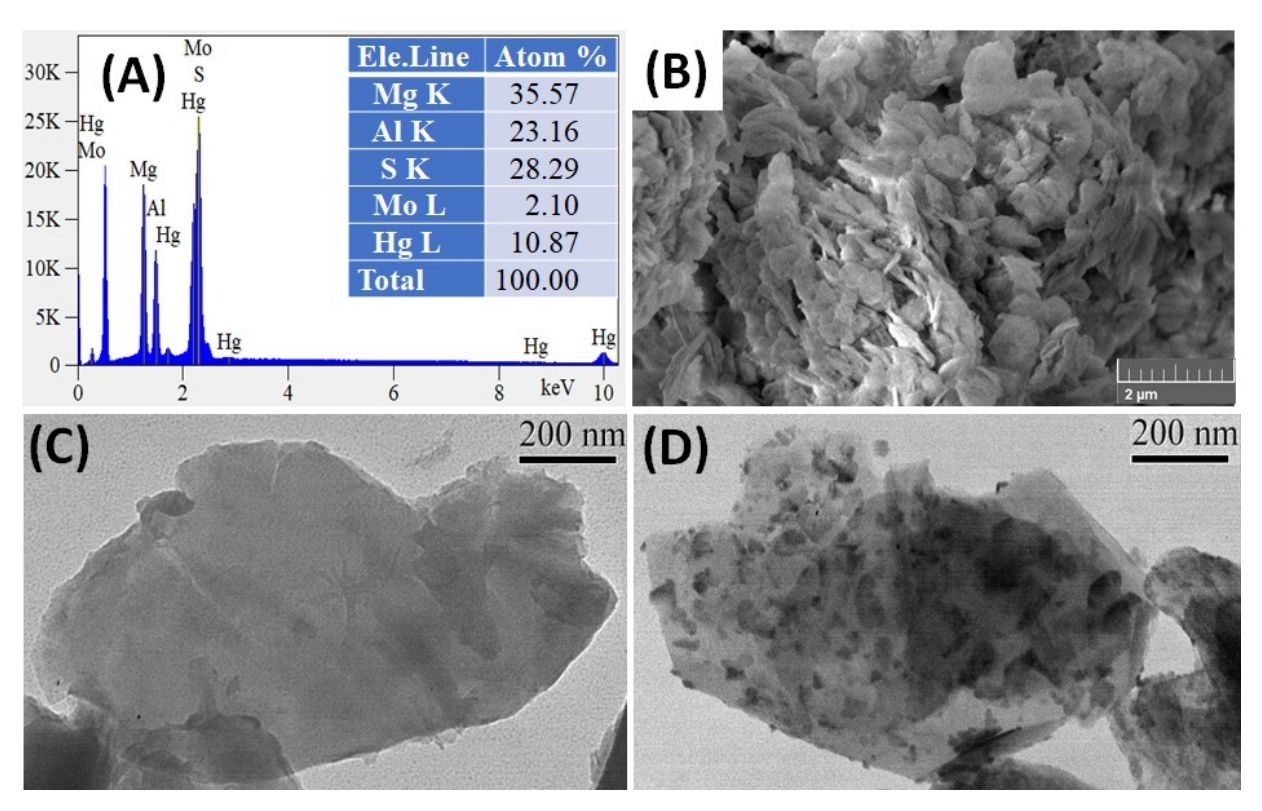


Figure 4. EDS spectrum and elemental compositions (A) show a significant amount of Hg in post-interacted LDH—Mo₃S₁₃; SEM image (B) of post-interacted LDH—Mo₃S₁₃ reveals the retention of the morphology; TEM images of pristine (C) show a clean surface of the platelike crystallites, while the post sorbed LDH—Mo₃S₁₃ (D) showing the formation of second phase due to sorption of gaseous Hg⁰.

To understand the detailed chemical states of the ions of sorbents, we analyzed the preand post-interacted LDH—Mo₃S₁₃ by X-ray photoelectron spectroscopy (Figure 5, Figure S4, and Table S2). XPS analysis of the post-interacted material reveals a doublet obtained at 100.05 and 104.10 eV ($\Delta = 4.05$ eV) corresponding to the $4f_{7/2}$ and $4f_{5/2}$ orbital energy of the Hg^{2+} ion, respectively^{71,72} (Figure 5B). This observation aligns with the results of XRD, Raman, and EDS analyses. Moreover, a comparable feature of the XPS shows that both the pristine and the postinteracted sorbent contains S²⁻ (at 161.29 and 162.44 eV); and S₂²⁻ (at 162.93 and 164.09 eV for $2p_{3/2}$ and $2p_{1/2}$ accordingly) (Figure 5C, D, and Table S2).^{72,73} The intensity of the S₂²⁻ peaks in the sample after interaction with mercury vapor becomes substantially weaker as compared to the pristine materials, while the intensity of the S²⁻ increases notably. This finding suggests the conversion of S₂²⁻ to S²⁻, the required sulfide species for HgS formation. Apart from this, both the pristine and post interacted LDH—Mo₃S₁₃ exhibit peaks corresponding to S⁶⁺ at about 168.20 and 169.35 eV for $2p_{3/2}$ and $2p_{1/2}$, accordingly (Figure 5C, D, and Table S2).^{72,73} However, the intensity of the S^{6+} peak in the post-interacting LDH— Mo_3S_{13} is substantially higher than that of the pristine materials. For the pristine LDH— Mo_3S_{13} , the weaker S^{6+} peak originated from the surface oxidation of di/polysulfide species, but the highly intense S^{6+} peak for the post interacted sorbent is attributed to air oxidation of the sulfides during the interactions with gaseous mercury in air. Hence, exposure of the sulfides in LDH— Mo_3S_{13} in the air under the experimental conditions leads to its oxidation and a subsequent formation of sulfate $[S^{VI}O_4]^{2-}$.

Moreover, XPS of the pristine LDH— Mo_3S_{13} reveals the tetravalent oxidation state of Mo, which is relevant to the Mo^{4+} oxidation state of the $Mo_3S_{13}^{2-}$ ions in pristine LDH— $[Mo^{IV}_3S(S_2)_6]$. A doublet of peaks was observed at 228.99 and 232.15 eV ($\Delta = 3.16$ eV) (Figure 5E) which correspond to the $3d_{5/2}$ and $3d_{3/2}$ of Mo^{4+} . 66,67,72,74 Instead, in the post-treated materials, Mo exists in two oxidation states, Mo^{4+} and Mo^{6+} (Figure 5F). The pair of doublets at 229.15 and 231.18 eV; 232.25 and 235.18 eV correspond to the $3d_{5/2}$ and $3d_{3/2}$ of Mo^{4+} and Mo^{6+} , respectively (Figure 5F). 72,74 The formation of Mo^{6+} in the post-treated sample can be understood by the oxidation of $Mo^{4+} \rightarrow Mo^{6+}$ during the gaseous mercury sorption processes in the air. 75

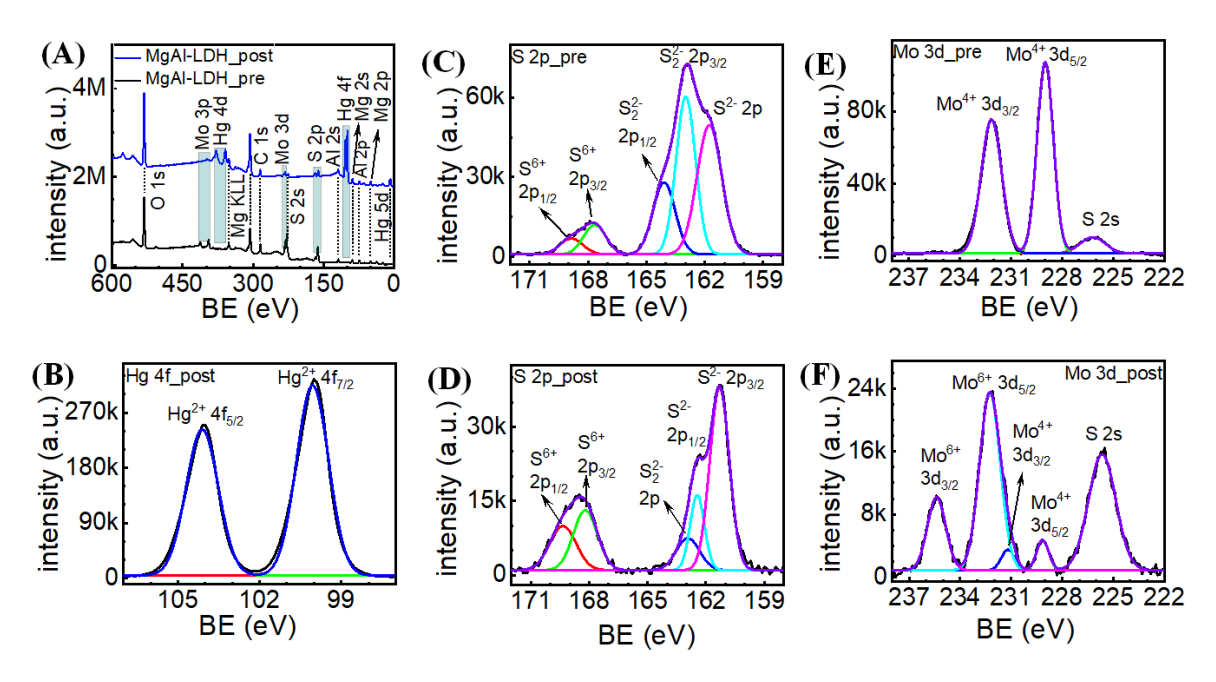


Figure 5. XPS survey peaks of pre- and post-Hg⁰-sorbed LDH—Mo₃S₁₃ (A) showing the Hg 4f peaks only in the post-interacted sample, (B) Comparison of XPS spectra of pre-(C and E) and post-(D and F) Hg⁰ sorbed LDH—Mo₃S₁₃ showing partial reduction of S₂²⁻ \rightarrow 2S²⁻ and oxidation of Mo⁴⁺ \rightarrow Mo⁶⁺ during Hg⁰ immobilization.

The generation of Mo^{6+} may likely result in the formation of $Mo^{VI}O_3$ and $Mo^{VI}O_4^{2-}$. As XRD does not detect any MoO_3 (Figure 3A), the creation of $Mo^{VI}O_4^{2-}$ is plausible. Additionally, the oxidation of sulfides of the Mo_3S_{13} group might produce gases like $S^{VI}O_3$ or $S^{VI}O_4^{2-}$ ions. If SO_3 is formed, it is expected to be released from the reactor. In contrast, if SO_4^{2-} is generated, it should remain in the post-interacted samples. Consequently, we believe that the oxidation of Mo and S leads to the creation of $S^{VI}O_4^{2-}$ and $Mo^{VI}O_4^{2-}$, and their formation is crucial for the stability of the LDH structure.

Quantum-Chemical Calculations

To further lend credence to the Hg^0 removal mechanism, we have performed quantum-chemical calculations to investigate the interaction of gaseous Hg^0 with $Mo_3S_{13}^{2-}$. For the DFT calculations, we considered the interactions of the $[Mo_3S_{13}]^{2-}$ ions with gaseous elemental Hg^0 , since our present experimental finding and previous reports suggest that sulfur-containing species is the active site for mercury immobilization. First, we have optimized the $Mo_3S_{13}^{2-}$ unit using the crystallographic data of the $(NH_4)_2Mo_3S_{13}^{48}$ following the procedure described in the computational methodology section. The optimized bond lengths along with the molecular structure of $Mo_3S_{13}^{2-}$ are depicted in Figure 6A. The calculated bond distances nicely agree with the corresponding crystallographic data, which lays the foundation for using the chosen computational methodology.

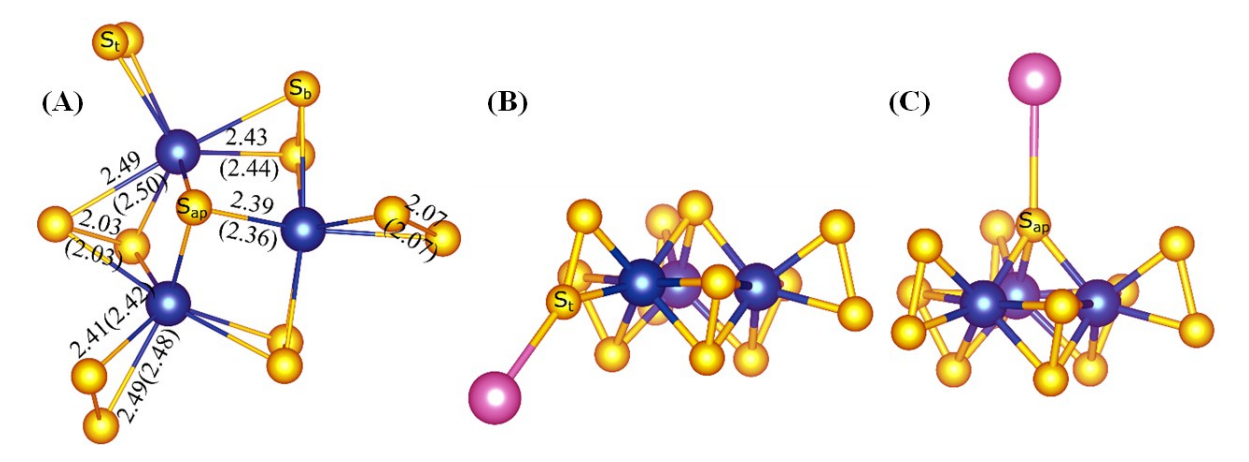


Figure 6. (A) Ball and stick representation of $Mo_3S_{13}^{2-}$ unit. The optimized Mo-S and S-S distances (Å) along with the corresponding experimental values (in the parenthesis) are shown along the bonds. (B) and (C) represent the strongest ($\Delta E_{ads} = -19 \text{ kJ/mol}$) and weakest ($\Delta E_{ads} = -8 \text{ kJ/mol}$) interactions predicted for the reaction of $Mo_3S_{13}^{2-}$ and Hg, respectively. The blue, yellow, and pink spheres represent Mo, S, and Hg atoms, respectively.

According to DFT calculation, the gaseous elemental Hg^0 atom primarily interacts with the S atom. The adsorption energy of the Hg^0 atom on the $Mo_3S_{13}^{2-}$ unit is calculated as $\Delta E_{ads} = E(Hg-Mo_3S_{13}^{2-}) - E(Mo_3S_{13}^{2-}) - E(Hg)$, where E is the total energy of the respective species. Depending on the spatial position of S at $Mo_3S_{13}^{2-}$, the adsorption energy varies from -8 kJ/mol to -19 kJ/mol. The terminal $(S_2^{2-})_t$, whose Mo-S distance is 2.490 Å has the strongest interaction with Hg^0 (Figure 6B). On the other hand, the weakest interaction is with the apical $(S^{2-})_{ap}$, whose Mo-S distance is 2.393 Å (Figure 6C). This finding is reasonable as weaker interaction of S with Mo (longer Mo-S distance) enables stronger interaction with Hg^0 and vice-versa. Finally, we have investigated the reaction energy for eq (1) and (2). Combining eq. (1) and (2) results as:

$$xHg(g) + LDH - (Mo_3S_{13})_y(s) + zO_2(g) \rightarrow xHgS(s) + LDH - (MoO_4)_{3y}(s) + LDH - (SO_4)_{13y-x}(s)$$
 Eq. 3

Like $Mo_3S_{13}^{2-}$, we have used SO_4^{2-} and MoO_4^{2-} to model LDH— SO_4 and LDH— MoO_4 , respectively. The calculated reaction energy of Eq. (3) is -4048 kJ/mol. Such a high negative reaction energy suggests a very low activation energy for this reaction which may lead to a spontaneous reaction between the gaseous Hg^0 and LDH— Mo_3S_{13} under the experimental conditions. The calculated energy further strengthens our experimental observation. The presence of oxygen (Eq. 3) plays an important role in the formation of HgS. While the exact mechanism is not known and may be more complex, the role of oxygen is further investigated by replacing a terminal sulfur, S_t of $Mo_3S_{13}^{2-}$ species by O as:

$$Hg(g) + LDH - Mo_3S_{13} + \frac{1}{2}O_2(g) = HgS(s) + LDH - Mo_3S_{12}O$$
 Eq. 4

The reaction energy of Eq. 4 is calculated as -124 kJ/mol, which supports the replacement of S by an O atom. The stronger bond energy of Mo—O (560 kJ/mol) compared to Mo—S (433 kJ/mol)⁷⁶ allows for the replacement of S by O atoms and eventually leads to the formation of HgS. To further confirm the role of oxygen in the formation of HgS, we have carried out a Hg⁰ sorption experiment in the absence of O₂ gas (O₂ and H₂O < 0.01 ppm) and in an ultrahigh pure N₂ atmosphere. The sorption capacity in such an inert gas environment is 226.84 mg/g, which is about 10-fold lower than the capacity obtained from the experiment carried out at atmospheric conditions.

SUMMARY AND OUTLOOK

Overall, our investigation demonstrates that LDH-[Mo₃S₁₃] is an exceedingly efficient sorbent for mercury vapor with a sorption capacity of 2.33×10³ mg/g and thus becomes the leading non-platinum mercury gas sorbent known to date. Numerous experiments, including XRD, EDS, and XPS, suggest that the immobilization of gaseous Hg⁰ occurs through the formation of HgS solid following the redox reactions involving elemental mercury and sulfide species. The experimental finding was further discarnate by DFT calculation revealing adsorption energy varies from -8 kJ/mol to -19 kJ/mol for the interactions between Hg⁰ and the sulfides. In contrast, the overall reaction energy for LDH-[Mo^{IV}₃S²-(S₂)²-₆] and gaseous Hg⁰ is found to be -4048 kJ/mol, suggesting a spontaneous reaction yielded the formation of HgS particles. Besides the thermodynamic stability of HgS, this finding suggests that mercury sulfide formation occurs through irreversible reactions, making LDH-Mo₃S₁₃ non-regenerative. Despite this fact, given its solution processability, scalability, cost-effectiveness, and ultra-high Hg⁰ sorption capacity, LDH-Mo₃S₁₃ has been revealed as a promising sorbent for gaseous Hg. This discovery implies that metal-sulfide intercalated layered double hydroxides are a promising class of sorbent for gaseous elemental mercury where the sulfide ions are the active sites to immobilize gaseous Hg. Thus, this investigation paves the way to design and develop new di/polysulfide-rich metal sulfide intercalated LDH and explore their efficiencies to develop a sorbent for gaseous elemental Hg^0 with superior capacity that can be utilized for natural gas purification as well as to remove gaseous Hg⁰ from flue gas and off-gas condensate nuclear waste. Future work on this class of materials should include the evaluation of their efficiencies under various experimental conditions besides designing innovative reactors set up under simulated conditions.

ACKNOWLEDGMENT

This work was supported by the NSF Division of Chemistry (CHE-2100797). A. A.

acknowledges financial support from NSF (CHE-2137662) and computational support from Penn

State's Institute for Computational and Data Science. BM acknowledges NSF (1826699) for the

financial support. The XPS work made use of the Keck-II facility of Northwestern University's

NUANCE Center, which has received support from the Soft and Hybrid Nanotechnology

Experimental (SHyNE) Resource (NSF ECCS-1542205); the MRSEC program (NSF DMR-

1121262) at the Materials Research Center; the International Institute for Nanotechnology (IIN);

the Keck Foundation; and the State of Illinois, through the IIN.

Supporting Information:

DTG analysis, XPS spectra and their assignment of pristine and post-sorbed LDH-Mo₃S₁₃,

XRD patterns of pre- and post-mercury sorbed LDH-NO₃ and (NH₄)₂Mo₃S₁₃, ICP-MS analysis of

LDH-Mo₃S₁₃- supplied as Supporting Information file.

AUTHOR CONTRIBUTIONS

This manuscript was written through the contributions of all authors. All authors have

approved the final version of the manuscript.

AUTHOR INFORMATION

Corresponding Author: muhammad.s.islam@jsums.edu

Department of Chemistry, Physics and Atmospheric Sciences

Jackson State University

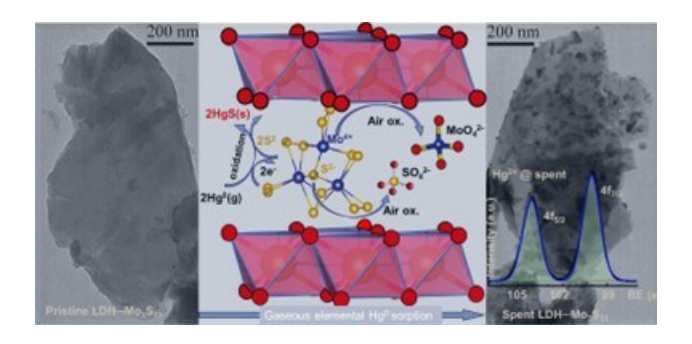
1400 J. R. Lynch Street

Jackson, MS 39217, USA

NOTES: The authors declare no competing financial interest

17

TOC Graphic:



Synopsys: This work reveals the importance of functionalizing two-dimensional layered double hydroxide nanoparticles with sulfide-rich molecular [Mo₃S(S₂)₆]²⁻ anions to enable a high-capacity redox-driven immobilization of gaseous mercury by forming HgS nanoparticles.

REFERENCES

- (1) Corbitt, E. S.; Jacob, D. J.; Holmes, C. D.; Streets, D. G.; Sunderland, E. M. Global Source–Receptor Relationships for Mercury Deposition Under Present-Day and 2050 Emissions Scenarios. *Environ. Sci. Technol.* **2011**, *45* (24), 10477–10484. https://doi.org/10.1021/es202496y.
- (2) Pirrone, N.; Cinnirella, S.; Feng, X.; Finkelman, R. B.; Friedli, H. R.; Leaner, J.; Mason, R.; Mukherjee, A. B.; Stracher, G. B.; Streets, D. G.; Telmer, K. Global Mercury Emissions to the Atmosphere from Anthropogenic and Natural Sources. *Atmospheric Chem. Phys.* **2010**, *10* (13), 5951–5964. https://doi.org/10.5194/acp-10-5951-2010.
- (3) Horowitz, H. M.; Jacob, D. J.; Zhang, Y.; Dibble, T. S.; Slemr, F.; Amos, H. M.; Schmidt, J. A.; Corbitt, E. S.; Marais, E. A.; Sunderland, E. M. A New Mechanism for Atmospheric Mercury Redox Chemistry: Implications for the Global Mercury Budget. *Atmospheric Chem. Phys.* **2017**, *17* (10), 6353–6371. https://doi.org/10.5194/acp-17-6353-2017.
- (4) Global Mercury Assessment 2018. UNEP UN Environment Programme. http://www.unep.org/resources/publication/global-mercury-assessment-2018 (accessed 2023-01-26).
- (5) US EPA, O. *Mercury Emissions: The Global Context*. https://www.epa.gov/international-cooperation/mercury-emissions-global-context (accessed 2023-02-05).
- (6) Streets, D. G.; Horowitz, H. M.; Jacob, D. J.; Lu, Z.; Levin, L.; Ter Schure, A. F. H.; Sunderland, E. M. Total Mercury Released to the Environment by Human Activities. *Environ. Sci. Technol.* **2017**, *51* (11), 5969–5977. https://doi.org/10.1021/acs.est.7b00451.
- (7) Li, T.; Mao, H.; Wang, Z.; Yu, J. Z.; Li, S.; Nie, X.; Herrmann, H.; Wang, Y. Field Evidence for Asian Outflow and Fast Depletion of Total Gaseous Mercury in the Polluted Coastal Atmosphere. *Environ. Sci. Technol.* **2023**, *57* (10), 4101–4112. https://doi.org/10.1021/acs.est.2c07551.

- (8) Shen, J.; Yin, R.; Algeo, T. J.; Svensen, H. H.; Schoepfer, S. D. Mercury Evidence for Combustion of Organic-Rich Sediments during the End-Triassic Crisis. *Nat. Commun.* **2022**, *13* (1), 1307. https://doi.org/10.1038/s41467-022-28891-8.
- (9) He, Y.; Shi, X.; Huffman, W. W.; Lamborg, C. H.; Mason, R. P. Description of a Dimethylmercury Automatic Analyzer for the High-Resolution Measurement of Dissolved Gaseous Mercury Species in Surface Ocean Waters. *Environ. Sci. Technol.* **2022**, *56* (18), 13076–13084. https://doi.org/10.1021/acs.est.2c02908.
- (10) Huggins, F. E.; Huffman, G. P.; Dunham, G. E.; Senior, C. L. XAFS Examination of Mercury Sorption on Three Activated Carbons. *Energy Fuels* **1999**, *13* (1), 114–121. https://doi.org/10.1021/ef9801322.
- (11) US EPA, O. 1990 Clean Air Act Amendment Summary. https://www.epa.gov/clean-air-act-overview/1990-clean-air-act-amendment-summary (accessed 2023-02-05).
- (12) Mason, R. P. Mercury Emissions from Natural Processes and Their Importance in the Global Mercury Cycle. In *Mercury Fate and Transport in the Global Atmosphere*; Mason, R., Pirrone, N., Eds.; Springer US: Boston, MA, 2009; pp 173–191. https://doi.org/10.1007/978-0-387-93958-2 7.
- (13) Esdaile, L. J.; Chalker, J. M. The Mercury Problem in Artisanal and Small-Scale Gold Mining. *Chem. Eur. J.* **2018**, *24* (27), 6905–6916. https://doi.org/10.1002/chem.201704840.
- (14) Streets, D. G.; Zhang, Q.; Wu, Y. Projections of Global Mercury Emissions in 2050. *Environ. Sci. Technol.* **2009**, *43* (8), 2983–2988. https://doi.org/10.1021/es802474j.
- (15) Pacyna, E. G.; Pacyna, J. M.; Steenhuisen, F.; Wilson, S. Global Anthropogenic Mercury Emission Inventory for 2000. *Atmos. Environ.* **2006**, *40* (22), 4048–4063. https://doi.org/10.1016/j.atmosenv.2006.03.041.
- (16) Introduction the Minamata Convention on Mercury For Global Mercury Pollution Prevention. Ministry of the Environment, Government of Japan. https://www.env.go.jp/en/chemi/mcm/intro.html (accessed 2023-01-26).
- (17) Chalkidis, A.; Jampaiah, D.; Hartley, P. G.; Sabri, Y. M.; Bhargava, S. K. Mercury in Natural Gas Streams: A Review of Materials and Processes for Abatement and Remediation. *J. Hazard. Mater.* **2020**, *382*, 121036. https://doi.org/10.1016/j.jhazmat.2019.121036.
- (18) Balasundaram, K.; Sharma, M. Technology for Mercury Removal from Flue Gas of Coal Based Thermal Power Plants: A Comprehensive Review. *Crit. Rev. Environ. Sci. Technol.* **2019**, *49* (18), 1700–1736. https://doi.org/10.1080/10643389.2019.1583050.
- (19) Behrouzi, A.; Zamecnik, J. Mercury Reduction and Removal from High Level Waste at the Defense Waste Processing Facility 12511; United States, 2012.
- (20) Taylor-Pashow, K. M. L.; Poirier, M.; McCabe, D. J. Bench Scale Experiments for the Remediation of Hanford Waste Treatment Plant Low Activity Waste Melter Off-Gas Condensate; SRNL-STI--2017-00322, 1377029; 2017; p SRNL-STI--2017-00322, 1377029. https://doi.org/10.2172/1377029.
- (21) Ma, S.; Shim, Y.; Islam, S. M.; Subrahmanyam, K. S.; Wang, P.; Li, H.; Wang, S.; Yang, X.; Kanatzidis, M. G. Efficient Hg Vapor Capture with Polysulfide Intercalated Layered Double Hydroxides. *Chem. Mater.* 2014, 26 (17), 5004–5011. https://doi.org/10.1021/cm5020477.
- (22) Gao, Y.; Zhang, Z.; Wu, J.; Duan, L.; Umar, A.; Sun, L.; Guo, Z.; Wang, Q. A Critical Review on the Heterogeneous Catalytic Oxidation of Elemental Mercury in Flue Gases. *Environ. Sci. Technol.* **2013**, *47* (19), 10813–10823. https://doi.org/10.1021/es402495h.

- (23) Yang, W.; Hussain, A.; Zhang, J.; Liu, Y. Removal of Elemental Mercury from Flue Gas Using Red Mud Impregnated by KBr and KI Reagent. *Chem. Eng. J.* **2018**, *341*, 483–494. https://doi.org/10.1016/j.cej.2018.02.023.
- (24) Zhou, R.; Wu, J.; Zhang, J.; Tian, H.; Liang, P.; Zeng, T.; Lu, P.; Ren, J.; Huang, T.; Zhou, X.; Sheng, P. Photocatalytic Oxidation of Gas-Phase Hg⁰ on the Exposed Reactive Facets of BiOI/BiOIO₃ Heterostructures. *Appl. Catal. B Environ.* **2017**, *204*, 465–474. https://doi.org/10.1016/j.apcatb.2016.11.013.
- (25) Liu, Z.; Yang, W.; Xu, W.; Liu, Y. Removal of Elemental Mercury by Bio-Chars Derived from Seaweed Impregnated with Potassium Iodine. *Chem. Eng. J.* **2018**, *339*, 468–478. https://doi.org/10.1016/j.cej.2018.01.148.
- (26) Mei, J.; Wang, C.; Kong, L.; Liu, X.; Hu, Q.; Zhao, H.; Yang, S. Outstanding Performance of Recyclable Amorphous MoS₃ Supported on TiO₂ for Capturing High Concentrations of Gaseous Elemental Mercury: Mechanism, Kinetics, and Application. *Environ. Sci. Technol.* **2019**, *53* (8), 4480–4489. https://doi.org/10.1021/acs.est.9b00464.
- (27) Kong, L.; Zou, S.; Mei, J.; Geng, Y.; Zhao, H.; Yang, S. Outstanding Resistance of H₂S-Modified Cu/TiO₂ to SO₂ for Capturing Gaseous Hg⁰ from Nonferrous Metal Smelting Flue Gas: Performance and Reaction Mechanism. *Environ. Sci. Technol.* **2018**, *52* (17), 10003–10010. https://doi.org/10.1021/acs.est.8b03484.
- (28) Xu, Y.; Luo, G.; Pang, Q.; He, S.; Deng, F.; Xu, Y.; Yao, H. Adsorption and Catalytic Oxidation of Elemental Mercury over Regenerable Magnetic Fe Ce Mixed Oxides Modified by Non-Thermal Plasma Treatment. *Chem. Eng. J.* **2019**, *358*, 1454–1463. https://doi.org/10.1016/j.cej.2018.10.145.
- (29) Yang, S.; Guo, Y.; Yan, N.; Wu, D.; He, H.; Xie, J.; Qu, Z.; Yang, C.; Jia, J. A Novel Multi-Functional Magnetic Fe–Ti–V Spinel Catalyst for Elemental Mercury Capture and Callback from Flue Gas. *Chem. Commun.* **2010**, *46* (44), 8377. https://doi.org/10.1039/c0cc02645j.
- (30) Yang, S.; Yan, N.; Guo, Y.; Wu, D.; He, H.; Qu, Z.; Li, J.; Zhou, Q.; Jia, J. Gaseous Elemental Mercury Capture from Flue Gas Using Magnetic Nanosized (Fe_{3-x}Mn_x)_{1-δ}O₄. *Environ. Sci. Technol.* **2011**, 45 (4), 1540–1546. https://doi.org/10.1021/es103391w.
- (31) Dang, H.; Liao, Y.; Ng, T. W.; Huang, G.; Xiong, S.; Xiao, X.; Yang, S.; Wong, P. K. The Simultaneous Centralized Control of Elemental Mercury Emission and Deep Desulfurization from the Flue Gas Using Magnetic Mn–Fe Spinel as a Co-Benefit of the Wet Electrostatic Precipitator. *Fuel Process. Technol.* **2016**, 142, 345–351. https://doi.org/10.1016/j.fuproc.2015.10.036.
- (32) Liu, Y.; Li, Y.; Xu, H.; Xu, J. Oxidation Removal of Gaseous Hg⁰ Using Enhanced-Fenton System in a Bubble Column Reactor. *Fuel* **2019**, *246*, 358–364. https://doi.org/10.1016/j.fuel.2019.03.018.
- (33) Removal of Mercury from Flue Gas Using Activated Carbon, Office of Mercury Management Environmental Health Department Ministry of the Environment, Japan, 2018. https://www.env.go.jp/council/07air-noise/y079-03/mat02 7.pdf).
- (34) Blythe, G. M. *Pilot Testing of Murcury Oxidation Catalysts for Upstream of Wet FGD Systems*; FC26-01NT41185--01, 793998; 2002; pp FC26-01NT41185--01, 793998. https://doi.org/10.2172/793998.
- (35) Oh, Y.; Morris, C. D.; Kanatzidis, M. G. Polysulfide Chalcogels with Ion-Exchange Properties and Highly Efficient Mercury Vapor Sorption. *J. Am. Chem. Soc.* **2012**, *134* (35), 14604–14608. https://doi.org/10.1021/ja3061535.

- (36) Li, H.; Zu, H.; Deng, Y.; He, W.; Yang, Z.; Yang, J.; Zhao, S.; Qu, W. Mechanisms of Gas-Phase Mercury Immobilized by Metal Sulfides from Combustion Flue Gas: A Mini Review. *Energy Fuels* **2022**, *36* (12), 6027–6037. https://doi.org/10.1021/acs.energyfuels.2c00904.
- (37) Zhao, H.; Yang, G.; Gao, X.; Pang, C. H.; Kingman, S. W.; Wu, T. Hg⁰ Capture over CoMoS/γ-Al₂O₃ with MoS₂ Nanosheets at Low Temperatures. *Environ. Sci. Technol.* **2016**, 50 (2), 1056–1064. https://doi.org/10.1021/acs.est.5b04278.
- (38) Xu, H.; Yuan, Y.; Liao, Y.; Xie, J.; Qu, Z.; Shangguan, W.; Yan, N. [MoS₄]²⁻ Cluster Bridges in Co–Fe Layered Double Hydroxides for Mercury Uptake from S–Hg Mixed Flue Gas. *Environ. Sci. Technol.* **2017**, *51* (17), 10109–10116. https://doi.org/10.1021/acs.est.7b02537.
- (39) Meyer, D. E.; Meeks, N.; Sikdar, S.; Hutson, N. D.; Hua, D.; Bhattacharyya, D. Copper-Doped Silica Materials Silanized With Bis-(Triethoxy Silyl Propyl)-Tetra Sulfide for Mercury Vapor Capture. *Energy Fuels* 2008, 22 (4), 2290–2298. https://doi.org/10.1021/ef8001873.
- (40) Meyer, D. E.; Sikdar, S. K.; Hutson, N. D.; Bhattacharyya, D. Examination of Sulfur-Functionalized, Copper-Doped Iron Nanoparticles for Vapor-Phase Mercury Capture in Entrained-Flow and Fixed-Bed Systems. *Energy Fuels* **2007**, *21* (5), 2688–2697. https://doi.org/10.1021/ef070120t.
- (41) Meeks, N. D.; Rankin, S.; Bhattacharyya, D. Sulfur-Functionalization of Porous Silica Particles and Application to Mercury Vapor Sorption. *Ind. Eng. Chem. Res.* 2010, 49 (10), 4687–4693. https://doi.org/10.1021/ie901580k.
- (42) Pitoniak, E.; Wu, C.-Y.; Mazyck, D. W.; Powers, K. W.; Sigmund, W. Adsorption Enhancement Mechanisms of Silica—Titania Nanocomposites for Elemental Mercury Vapor Removal. *Environ. Sci. Technol.* 2005, 39 (5), 1269–1274. https://doi.org/10.1021/es049202b.
- (43) Yuan, Y.; Xu, H.; Liu, W.; Chen, L.; Quan, Z.; Liu, P.; Qu, Z.; Yan, N. Morphology-Controlled Synthesis and Sulfur Modification of 3D Hierarchical Layered Double Hydroxides for Gaseous Elemental Mercury Removal. *J. Colloid Interface Sci.* **2019**, *536*, 431–439. https://doi.org/10.1016/j.jcis.2018.10.062.
- (44) Yao, Y.; Velpari, V.; Economy, J. Design of Sulfur Treated Activated Carbon Fibers for Gas Phase Elemental Mercury Removal. *Fuel* **2014**, *116*, 560–565. https://doi.org/10.1016/j.fuel.2013.08.063.
- (45) Korpiel, J. A.; Vidic, R. D. Effect of Sulfur Impregnation Method on Activated Carbon Uptake of Gas-Phase Mercury. *Environ. Sci. Technol.* **1997**, *31* (8), 2319–2325. https://doi.org/10.1021/es9609260.
- (46) Hsi, H.-C.; Rood, M. J.; Rostam-Abadi, M.; Chen, S.; Chang, R. Mercury Adsorption Properties of Sulfur-Impregnated Adsorbents. *J. Environ. Eng.* 2002, 128 (11), 1080–1089. https://doi.org/10.1061/(ASCE)0733-9372(2002)128:11(1080).
- (47) Celik, A.; Li, D.; Quintero, M. A.; Taylor-Pashow, K. M. L.; Zhu, X.; Shakouri, M.; Roy, S. C.; Kanatzidis, M. G.; Arslan, Z.; Blanton, A.; Nie, J.; Ma, S.; Han, F. X.; Islam, S. M. Removal of CrO₄²⁻, a Nonradioactive Surrogate of ⁹⁹TcO₄⁻, Using LDH–Mo₃S₁₃ Nanosheets. *Environ. Sci. Technol.* **2022**, *56* (12), 8590–8598. https://doi.org/10.1021/acs.est.1c08766.
- (48) Islam, S. M.; Cain, J. D.; Shi, F.; He, Y.; Peng, L.; Banerjee, A.; Subrahmanyam, K. S.; Li, Y.; Ma, S.; Dravid, V. P.; Grayson, M.; Kanatzidis, M. G. Conversion of Single Crystal (NH₄)₂Mo₃S₁₃·H₂O to Isomorphic Pseudocrystals of MoS₂ Nanoparticles. *Chem. Mater.* **2018**, *30* (11), 3847–3853. https://doi.org/10.1021/acs.chemmater.8b01247.

- (49) Yang, L.; Xie, L.; Chu, M.; Wang, H.; Yuan, M.; Yu, Z.; Wang, C.; Yao, H.; Islam, S. M.; Shi, K.; Yan, D.; Ma, S.; Kanatzidis, M. G. Mo₃S₁₃²⁻ Intercalated Layered Double Hydroxide: Highly Selective Removal of Heavy Metals and Simultaneous Reduction of Ag ⁺ Ions to Metallic Ag ⁰ Ribbons. *Angew. Chem. Int. Ed.* **2022**, *61* (1), e202112511. https://doi.org/10.1002/anie.202112511.
- (50) Kresse, G.; Hafner, J. Norm-Conserving and Ultrasoft Pseudopotentials for First-Row and Transition Elements. *J. Phys. Condens. Matter* **1994**, *6* (40), 8245–8257. https://doi.org/10.1088/0953-8984/6/40/015.
- (51) Kresse, G.; Furthmüller, J. Efficiency of Ab-Initio Total Energy Calculations for Metals and Semiconductors Using a Plane-Wave Basis Set. *Comput. Mater. Sci.* **1996**, *6* (1), 15–50. https://doi.org/10.1016/0927-0256(96)00008-0.
- (52) Kresse, G.; Joubert, D. From Ultrasoft Pseudopotentials to the Projector Augmented-Wave Method. *Phys. Rev. B* **1999**, *59* (3), 1758–1775. https://doi.org/10.1103/PhysRevB.59.1758.
- (53) Perdew, J. P.; Burke, K.; Ernzerhof, M. Generalized Gradient Approximation Made Simple. *Phys. Rev. Lett.* **1996**, 77 (18), 3865–3868. https://doi.org/10.1103/PhysRevLett.77.3865.
- (54) Monkhorst, H. J.; Pack, J. D. Special Points for Brillouin-Zone Integrations. *Phys. Rev. B* **1976**, *13* (12), 5188–5192. https://doi.org/10.1103/PhysRevB.13.5188.
- (55) Müller, A.; Sarkar, S.; Bhattacharyya, R. G.; Pohl, S.; Dartmann, M. Directed Synthesis of [Mo₃S₁₃]²⁻, an Isolated Cluster Containing Sulfur Atoms in Three Different States of Bonding. *Angew. Chem. Int. Ed. Engl.* **1978**, *17* (7), 535–535. https://doi.org/10.1002/anie.197805351.
- (56) Zhang, L.; Wang, H.; Zhang, Q.; Wang, W.; Yang, C.; Du, T.; Yue, T.; Zhu, M.; Wang, J. Demand-Oriented Construction of Mo₃3S₁₃-LDH: A Versatile Scavenger for Highly Selective and Efficient Removal of Toxic Ag(I), Hg(II), As(III), and Cr(VI) from Water. *Sci. Total Environ.* **2022**, *820*, 153334. https://doi.org/10.1016/j.scitotenv.2022.153334.
- (57) Yuan, M.; Yao, H.; Xie, L.; Liu, X.; Wang, H.; Islam, S. M.; Shi, K.; Yu, Z.; Sun, G.; Li, H.; Ma, S.; Kanatzidis, M. G. Polypyrrole–Mo₃S₁₃: An Efficient Sorbent for the Capture of Hg²⁺ and Highly Selective Extraction of Ag⁺ over Cu²⁺. *J. Am. Chem. Soc.* **2020**, *142* (3), 1574–1583. https://doi.org/10.1021/jacs.9b12196.
- (58) Xie, X.; Chen, H.; Liu, X.; Xiang, K.; Liu, H. Achieving Large-Capability Adsorption of Hg⁰ in Wet Scrubbing by Defect-Rich Colloidal Copper Sulfides under High-SO₂ Atmosphere. *Materials* **2023**, *16* (8), 3157. https://doi.org/10.3390/ma16083157.
- (59) Subrahmanyam, K. S.; Malliakas, C. D.; Sarma, D.; Armatas, G. S.; Wu, J.; Kanatzidis, M. G. Ion-Exchangeable Molybdenum Sulfide Porous Chalcogel: Gas Adsorption and Capture of Iodine and Mercury. *J. Am. Chem. Soc.* **2015**, *137* (43), 13943–13948. https://doi.org/10.1021/jacs.5b09110.
- (60) Oh, Y.; Bag, S.; Malliakas, C. D.; Kanatzidis, M. G. Selective Surfaces: High-Surface-Area Zinc Tin Sulfide Chalcogels. *Chem. Mater.* **2011**, *23* (9), 2447–2456. https://doi.org/10.1021/cm2003462.
- (61) Liu, C.; Xiang, K.; Li, J.; Li, C.; Liu, L.; Shen, F.; Liu, H. Edge-Enriched Molybdenum Disulfide Ultrathin Nanosheets with a Widened Interlayer Spacing for Highly Efficient Gaseous Elemental Mercury Capture. *Environ. Sci. Technol.* **2023**, *57* (26), 9884–9893. https://doi.org/10.1021/acs.est.3c03065.
- (62) Li, H.; Yang, Q.; Qu, W.; Feng, Y.; Leng, L.; Zhao, J.; Meng, F.; Yang, Z.; Yang, J. Facile Preparation of Nanosized Copper Sulfide Functionalized Macroporous Skeleton for Efficient

- Vapor-Phase Mercury Sequestration. *Chem. Eng. J.* **2021**, 419, 129561. https://doi.org/10.1016/j.cej.2021.129561.
- (63) Xu, T.; Wei, J.; He, P.; Wu, J.; Chen, N.; Shi, E.; Pan, C.; Zhao, X.; Zhang, Y. CuS-Doped Ti₃C₂ MXene Nanosheets for Highly Efficient Adsorption of Elemental Mercury in Flue Gas. *Energy Fuels* **2022**, *36* (5), 2503–2514. https://doi.org/10.1021/acs.energyfuels.1c03705.
- (64) Kyzas, G. Z.; Travlou, N. A.; Deliyanni, E. A. The Role of Chitosan as Nanofiller of Graphite Oxide for the Removal of Toxic Mercury Ions. *Colloids Surf. B Biointerfaces* **2014**, *113*, 467–476. https://doi.org/10.1016/j.colsurfb.2013.07.055.
- (65) Marimuthu, G.; Arivanandhan, M.; Vedhi, C. Chemical Vapor Deposition of β-HgS Nanoparticles From a Precursor, Bis(Cinnamylpiperazinedithiocarbamato) Mercury(II). Synth. React. Inorg. Met.-Org. Nano-Met. Chem. 2015, 45 (2), 217–224. https://doi.org/10.1080/15533174.2013.831884.
- (66) Kibsgaard, J.; Jaramillo, T. F.; Besenbacher, F. Building an Appropriate Active-Site Motif into a Hydrogen-Evolution Catalyst with Thiomolybdate [Mo₃S₁₃]²⁻ Clusters. *Nat. Chem.* **2014**, *6* (3), 248–253. https://doi.org/10.1038/nchem.1853.
- (67) Tran, P. D.; Tran, T. V.; Orio, M.; Torelli, S.; Truong, Q. D.; Nayuki, K.; Sasaki, Y.; Chiam, S. Y.; Yi, R.; Honma, I.; Barber, J.; Artero, V. Coordination Polymer Structure and Revisited Hydrogen Evolution Catalytic Mechanism for Amorphous Molybdenum Sulfide. *Nat. Mater.* **2016**, *15* (6), 640–646. https://doi.org/10.1038/nmat4588.
- (68) Pham, C. V.; Zana, A.; Arenz, M.; Thiele, S. [Mo₃S₁₃]²⁻ Cluster Decorated Sulfur-doped Reduced Graphene Oxide as Noble Metal-Free Catalyst for Hydrogen Evolution Reaction in Polymer Electrolyte Membrane Electrolyzers. *ChemElectroChem* **2018**, *5* (18), 2672–2680. https://doi.org/10.1002/celc.201800719.
- (69) Diemann, E.; Mueller, A.; Aymonino, P. J. Thermal Decomposition of (NH₄)₂[Mo₃S(S₂)₆] nH₂O. Z. Fuer Anorg. Allg. Chem. **1981**, 479 (8), 191–198. https://doi.org/10.1002/zaac.19814790824.
- (70) Frost, R. L.; Martens, W. N.; Kloprogge, J. T. Raman Spectroscopic Study of Cinnabar (HgS), Realgar (As4S₄), and Orpiment (As₂S₃) at 298 and 77K. *Neues Jahrb. Für Mineral. Monatshefte* **2002**, 2002 (10), 469–480. https://doi.org/10.1127/0028-3649/2002/2002-0469.
- (71) Biesinger, M. X-ray Photoelectron Spectroscopy (XPS) Reference Pages of Mercury. http://www.xpsfitting.com/search?q=mercury (accessed 2022-12-29).
- (72) Moulder, J. F.; Stickle, W. F.; Sobol, P. E.; Bomben, K. D. *Handbook of X-Ray Photoelectron Spectroscopy*, 2nd Edition.; Perkin-Elmer Corporation, 1992, p112.
- (73) Biesinger, M. *X-ray Photoelectron Spectroscopy (XPS) Reference Pages of Sulphur*. http://www.xpsfitting.com/search/label/Sulphur (accessed 2022-12-29).
- (74) Biesinger, M. *X-ray Photoelectron Spectroscopy (XPS) Reference Pages of Molybdenym*. http://www.xpsfitting.com/search/label/Molybdenum (accessed 2022-12-29).
- (75) Schmidt, D. P. Thermodynamische Analyse der Existenzbereiche fester Phasen-Prinzipien der Syntheseplanung in der anorganischen Festkörperchemie. **2008**.
- (76) Liu, X.; Cao, D.; Yang, T.; Li, H.; Ge, H.; Ramos, M.; Peng, Q.; Dearden, A. K.; Cao, Z.; Yang, Y.; Li, Y.-W.; Wen, X.-D. Insight into the Structure and Energy of Mo₂₇S_xO_y Clusters. *RSC Adv.* **2017**, *7* (16), 9513–9520. https://doi.org/10.1039/C6RA26264C.